Air-water interface boundary condition for the numerical evaporation rate prediction of a horizontal water span under different convection regimes

Quentin Royer, Romain Guibert, Pierre Horgue, Adam Swadling, Gérald Debenest

International Journal of Heat and Mass Transfer 226 (2024) 125438

Contents lists available at ScienceDirect

International Journal of Heat and Mass Transfer

journal homepage: www.elsevier.com/locate/ijhmt

Air-water interface boundary condition for the numerical evaporation rate prediction of a horizontal water span under different convection regimes

Quentin Royer [a,b,*], Romain Guibert [a], Pierre Horgue [a], Adam Swadling [b], Gérald Debenest [a]

[a] Institut de Mécanique des Fluides de Toulouse (IMFT) - Université de Toulouse, CNRS-INPT-UPS, Toulouse, France
[b] Safetykleen, La Courneuve, France

ARTICLE INFO

Keywords:
Drying
Evaporation
Water vapor flux
Boundary condition

ABSTRACT

This paper conducts a comprehensive analysis of the existing numerical models addressing the dynamics of water vapor flux across the air-water interface. Additionally, it introduces a novel model based on the empirical friction velocity of the air over a water surface. This new model is used to predict evaporation rates, especially in the context of wind tunnel experiments where water tanks are subjected to controlled drying conditions. Then, these predictions are compared to both the empirically measured evaporation rates and those generated by other numerical models. A wide range of configurations are simulated to cover the different convection regimes. Overall, these simulations show good agreement between the model's predictions and the observed experimental measurements of evaporation rates, underscoring its robustness and reliability. One notable advantage of this model is its remarkable independence from the convection regime, setting it apart from traditional empirical correlations that typically exhibit such dependencies.

1. Introduction

The mass transfer between a water surface and the surrounding air environment is predominant in many situations, including industrial processes. Understanding and predicting the evaporation process is crucial in some of these cases, such as the sizing of HVAC (Heating, Ventilation and Air Conditioning) equipment in buildings [1,2] or the optimization of drying processes [3].

The mass transfer of water vapor in the air is a specific case of the mass transfer between two immiscible fluids, described by Fick's laws [4]. These laws are analogous to Fourier's heat transfer laws, where the thermal diffusivity is replaced by a mass diffusivity and the temperature gradient is replaced by a concentration gradient.

Since the 19th century, several authors developed empirical correlations to predict the water evaporation flux from a horizontal water surface based on Dalton's law [5]. This law relates the evaporation rate to the difference between the partial vapor pressure close to the water surface and the ambient partial vapor pressure. These correlations are valid under specific conditions (on the geometry, wind velocity, temperature, and humidity range), and some of them are reported by Aldarabseh [6]. Because of the range of validity of these correlations, it may be troublesome to predict the water evaporation of a horizontal water span.

Some authors assessed the problem with numerical models. Ciuman and Lipska [7] deal with the humidity distribution induced by the evaporation of an indoor swimming pool, where empirical correlations are used to predict the water evaporation. Limane et al. [8] carried out a similar study, focusing on heat comfort rather than the water evaporation rate. Raimundo et al. [9] and Blázquez et al. [10] both conducted experimental setups and simulations to evaluate the evaporation of a water tank in a wind tunnel. In the latter study, they developed specific water surface boundary conditions that operate independently of empirical correlations. These boundary conditions, discussed in more detail below, incorporate the physics of evaporation through various approaches. It's worth noting that these boundary conditions may not inherently encompass the full spectrum of convection regimes without parameter calibration.

In the present work, we propose and implement a novel boundary condition to predict the water evaporation of a horizontal water surface, tested across multiple experimental setups, as documented in the existing literature. The main difference with the previous models lies in the computation of the mixture velocity near the air-water interface. In our approach, this velocity is estimated through the empirical friction ve-

* Corresponding author.
E-mail address: quentin.royer@toulouse-inp.fr (Q. Royer).

https://doi.org/10.1016/j.ijheatmasstransfer.2024.125438
Received 7 November 2023; Received in revised form 31 December 2023; Accepted 11 March 2024
Available online 24 March 2024

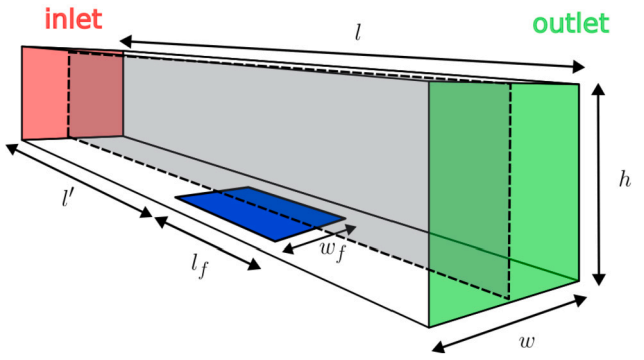

Fig. 1. Representative scheme of a typical experimental setup where the grey plane corresponds to that used for 2D numerical configurations.

Table 1
Dimensions of the wind tunnel for each experimental configuration. Only Raimundo et al. [9]'s setup has $w \neq w_f$.

Case	Inan and Atayılmaz [18]	Blázquez et al. [30] Gallero et al. [32] Blázquez et al. [22]	Raimundo et al. [9]
l [m]	1.8	1	3.3
h [m]	0.4	0.3	0.4
w [m]	0.4	0.3	0.4
l' [m]	0.547	0.65	1.8
l_f [m]	0.42875	0.325	0.15
w_f [m]	0.4	0.3	0.15

locity at the air-water interface [11–14]. While empirical correlations for evaporation flux may exhibit variations and discrepancies among different authors, it's noteworthy that the empirical friction velocity remains consistent and unchanged across these studies.
Hereafter, a detailed description of the simulated setups is presented, followed by the physical and numerical methodologies.

2. Materials and methods

2.1. Configurations

The studied configurations are wind tunnels with a low-high water reservoir in front of the tunnel opening. In the diverse experimental studies in the literature, the evaporation rate of the water contained within the reservoir tank is quantified under a variety of flow conditions. This measurement is accomplished by monitoring the evolution of the mass of evaporated water using a balance. The Fig. 1 is a comprehensive scheme of a typical setup. The water tank is always placed along the symmetry axis of the wind tunnel. If the water tank has the same width as the wind tunnel (i.e. $w_f = w$), it can be reasonably assumed that the flow is independent of the width, thus enabling us to conduct two-dimensional (2D) simulations along the length of the wind tunnel. On Fig. 1, the grey plane is the one used for the assumed 2D cases. The Table 1 sums up the dimensions of the different experimental cases studied. Each experimental setup has its own range of temperature, relative humidity and wind velocity, all influencing the rate of water evaporation. These diverse ranges of physical parameters can be translated into corresponding ranges of dimensionless numbers, including:

- The Reynolds number Re_h, which is the ratio between inertial and viscous forces,

$$Re_h = \frac{U_\infty h}{\nu} \tag{1}$$

based on the tunnel height h [m], U_∞ the magnitude of the inlet velocity [m.s^{-1}] and ν the laminar kinematic viscosity of the mixture [m^2.s^{-1}].

- The temperature Richardson number Ri_T, which is the ratio between the gravitational potential energy of the fluid induced by a temperature difference and the fluid's kinetic energy,

$$Ri_T = \frac{g\beta_T(T_{ws} - T_\infty)l_f}{U_\infty^2} \tag{2}$$

with g the magnitude of the gravity acceleration [m.s^{-2}], β_T the thermal expansion coefficient [K^{-1}], T_{ws} the temperature at the water surface [K] and T_∞ the inlet temperature [K].
- The concentration Richardson number Ri_C, which is the ratio between the gravitational potential energy of the fluid induced by a vapor concentration difference and the fluid's kinetic energy,

$$Ri_C = \frac{g\beta_C(Y_{ws} - Y_\infty)l_f}{U_\infty^2} \tag{3}$$

with β_C the concentration expansion coefficient [−], Y_{ws} the saturation water vapor mass fraction in the air at water surface temperature [−] and Y_∞ the inlet water vapor mass fraction [−].

The transition to turbulence in square channels occurs at $Re_c = 1460$ and for smaller Reynolds values in the case of rectangular channels [15]. The usual bounds for the forced, mixed, and natural convection regimes, are the same for both Richardson numbers defined. They assume to respectively be chosen as $Ri_{forced} < 0.1$, $0.1 < Ri_{mixed} < 10$ and $Ri_{natural} > 10$ [16].
The range of dimensionless numbers explored in the present study is presented in Fig. 2. For a fixed Reynolds number, the temperature of the water is changed (and so are the temperature and concentration Richardson numbers), creating plateaus. These plateaus are better seen on Fig. 3a because of the logarithmic horizontal axis. As illustrated in Fig. 2(b), it's worth noting that the temperature Richardson number can be negative when the water tank's temperature is lower than the air temperature, which is a common scenario in the investigation of indoor swimming pools. In such cases, evaporation is primarily driven by the difference in water vapor concentration. Most of the simulated cases are operating within the forced and mixed convection regimes. There are only two sets of data falling under the natural convection regime, as discussed in detail later in section 3.3. The studied setups have been chosen because they cover a wide range of flow conditions, and details about the inlet flow conditions are available, which might not always be the case [17]. In Inan and Atayılmaz [18] and Blázquez et al. [10], the vapor pressure difference is mainly controlled by the inlet air temperature and humidity whereas in Raimundo et al. [9], it is mainly controlled by the water temperature.

2.2. Mathematical model

The inflow fluid is composed of a mixture of dry air and water vapor. It is treated as thermally expansible, although it is considered incompressible following Boussinesq's approximation [19]. The consideration of density change is then confined to its interaction with gravity, thus avoiding the need to solve a compressible flow. This change in density becomes apparent when the mixture encounters temperature and/or vapor concentration gradients.
Water vapor and dry air are assumed to be non-reactive fluids. Furthermore, since the concentration of water vapor is consistently low in dry air, it is also assumed that both fluids share the same temperature and velocity fields. As stated by Raimundo et al. [9] and Limane et al. [8], the radiative transfer between the walls and the water pan can be neglected and since the mass flow induced by the temperature and/or the concentration gradient is small, the Soret and Dufour effects are also negligible.
Therefore, we will address the following system of equations:

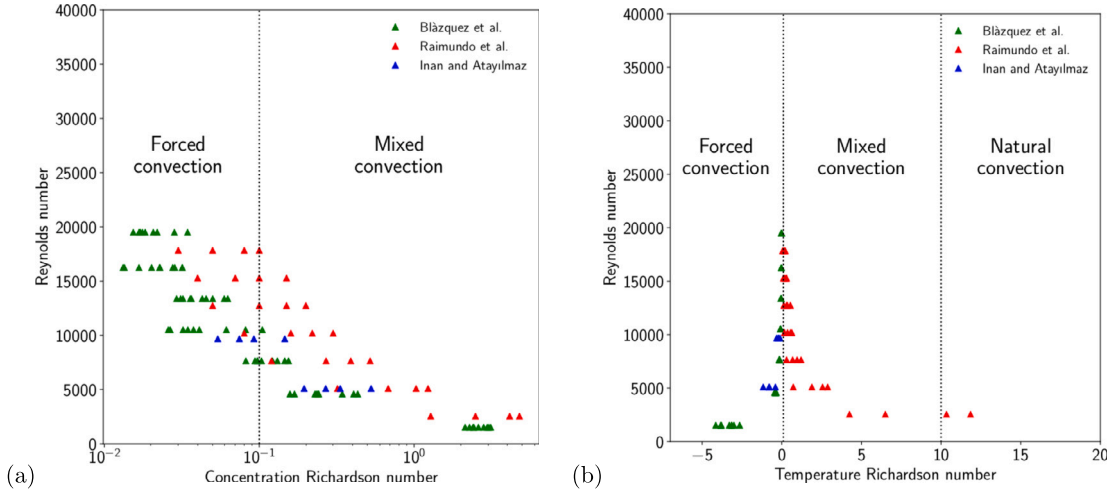

Fig. 2. Range of Reynolds and Richardson numbers explored, with the Richardson number being based on (a) the water vapor concentration difference and (b) the temperature difference. The dotted lines are the separation of the prevailing convection regimes.

– The mass conservation

$$\nabla \cdot \mathbf{u} = 0 \tag{4}$$

where $\mathbf{u}$ is the velocity vector field [m.s^{-1}];

– The momentum conservation

$$\frac{\partial \mathbf{u}}{\partial t} + (\nabla \mathbf{u}) \cdot \mathbf{u} = -\frac{1}{\rho}\nabla p - \mathbf{g}\beta_T(T - T_\infty) - \mathbf{g}\beta_C(Y - Y_\infty) + \nu_{eff}\Delta \mathbf{u} \tag{5}$$

where t is the time [s], ρ the mixture density [kg.m^{-3}], p the pressure [Pa], $\mathbf{g}$ the gravity acceleration vector [m.s^{-2}], T the temperature [K], Y the vapor mass fraction [−], $\nu_{eff} = \nu + \nu_t$ the effective kinematic viscosity [m^2.s^{-1}] and ν_t the turbulent kinematic viscosity [m^2.s^{-1}];

– The energy conservation

$$\frac{\partial T}{\partial t} + (\nabla T) \cdot \mathbf{u} = \alpha_{eff}\Delta T \tag{6}$$

where $\alpha_{eff} = \alpha + \alpha_t$ is the effective thermal diffusivity [m^2.s^{-1}], α the laminar thermal diffusivity [m^2.s^{-1}] and α_t the turbulent thermal diffusivity [m^2.s^{-1}];

– And the water vapor concentration conservation

$$\frac{\partial Y}{\partial t} + (\nabla Y) \cdot \mathbf{u} = D_{eff}\Delta Y \tag{7}$$

where $D_{eff} = D + D_t$ is the effective water vapor mass diffusivity in air [m^2.s^{-1}], D the laminar water vapor mass diffusivity in air [m^2.s^{-1}] and D_t the turbulent water vapor mass diffusivity in air [m^2.s^{-1}].

The laminar diffusivity of water vapor in air is evaluated following Lienhard [20]:

$$D = 1.87\,10^{-10}\left(\frac{T^{2.072}}{p}\right). \tag{8}$$

The overall minimum Reynolds number of the simulated setups is 1529 (Fig. 2), *i.e.* higher than Re_c. As a result, a turbulence model can be employed to simulate the turbulent structures within the flow. Due to its accuracy and stability, the SST (Shear-Stress Transport) RANS (Reynolds Averaged Navier-Stokes) model has been chosen [21].

The turbulent thermal diffusivity α_t and the turbulent mass diffusivity of water vapor in air D_t are both estimated using dimensionless numbers, the turbulent Prandtl number Pr_t

$$Pr_t = \frac{\nu_t}{\alpha_t}, \tag{9}$$

and the turbulent Schmidt number Sc_t

$$Sc_t = \frac{\nu_t}{D_t}. \tag{10}$$

Usually, the turbulent Prandtl number is set equal to 0.85 and the turbulent Schmidt number to 0.7. Under the flow configurations considered, Blázquez et al. [22] and Raimundo et al. [9] state that the standard value of the turbulent Schmidt number is not adequate and is locally variable. Tominaga and Stathopoulos [23] compile works on the turbulent Schmidt number across various flow configurations, indicating that an optimal range of 0.2 to 1.3 may enhance agreement with experimental data. In this current study, the values of Pr_t and Sc_t have been fixed at 0.85 and 0.2 respectively, following Blázquez et al. [22] recommendations, as they give the best overall agreement with the experimental data.

When using a RANS model, the turbulence decay close to the walls needs to be correctly described [24]. Jayatilleke's heat transfer wall function has been chosen to compute the turbulent heat transfer close to the walls and at the air-water interface [25]. Given that heat and mass transfer convection exhibit similar behavior in the context of air-water heat and mass transfer [4,9], the turbulent mass transfer wall function is computed in a manner analogous to the heat transfer wall function. This is achieved by substituting the (turbulent) Prandtl number with the (turbulent) Schmidt number, as previously implemented by Raimundo et al. [9]. The turbulent kinetic energy, the specific dissipation rate and the turbulent viscosity wall functions are standard wall functions.

The aim of the present work is to propose a numerical model able to predict the water evaporation flux. In various experiments, the authors measured the water mass loss from the tank with an electronic balance, allowing them to calculate the evaporation rate. Numerically, the water vapor flux is determined by equating the inlet and the outlet vapor mass flux:

$$J = \frac{1}{\Delta t}\left(\left(\iiint_\Omega \rho Y \, d\Omega\right)^{t_n} - \left(\iiint_\Omega \rho Y \, d\Omega\right)^{t_{n-1}}\right) + \iint_{\partial\Omega_{out}} \rho Y \mathbf{u}\cdot\mathbf{n}_{out} \, d\partial\Omega_{out} - \iint_{\partial\Omega_{in}} \rho Y \mathbf{u}\cdot\mathbf{n}_{in} \, d\partial\Omega_{in} \tag{11}$$

where J is the water vapor mass flux in the air [kg.m^{-2}.s^{-1}], t_n the time at iteration n [s], Ω is the control volume [m^3], $\partial\Omega_{out}$ is Ω's outlet boundary surface [m^2], $\mathbf{n}_{out}$ is $\partial\Omega_{out}$'s normal vector pointing outwards [m], $\partial\Omega_{in}$ is Ω's inlet boundary surface [m^2] and $\mathbf{n}_{in}$ is $\partial\Omega_{in}$'s normal vector pointing outwards [m].
It is important to notice that the first term of Equation (11) tends towards zero when reaching the convergence.

2.3. Boundary conditions

The walls are considered impermeable, adiabatic and unmovable. Since none of the authors measured the inlet turbulence intensity, an inlet turbulence level of 6% has been assumed as in Raimundo et al. [9]'s work. The inflow conditions (velocity, temperature and vapor concentration) are given by the experimental conditions while the pressure at the outlet is fixed at 1 atm. Since the water pan is centered along the symmetry axis of the wind tunnel, the tunnel can be divided in half with a symmetry boundary condition, reducing the computational expense of the simulation. This assumption is discussed later in section 3.3.
Near the air-water interface, a thin saturated air layer exists [26] and, since only the air-vapor mixture is solved, the temperature at the interface boundary is set according to the water's surface temperature. The temperature of the water pan being controlled by an electrical resistance, it is assumed that the temperature of the water surface is also controlled by the latter. The vapor mass fraction at the interface Y_s is then deduced from the saturation pressure, denoted p_s, based on this temperature, following Buck [27] and from the ideal gas assumption:

$$p_s = 0.61121 \exp\left(\left(18.678 - \frac{T}{234.5}\right)\left(\frac{T}{257.14+T}\right)\right) \tag{12}$$

$$Y_s = \frac{p_s W_w}{W_a(p_{atm} - p_s) + W_w p_s} \tag{13}$$

where W_w is the water molecular weight [kg.mol^{-1}], W_a is the air molecular weight [kg.mol^{-1}] and p_{atm} is the atmospheric pressure [Pa].
When it comes to the velocity boundary condition, it has been assumed by Raimundo et al. [9] that the tangential velocity of the mixture close to the water surface (along the streamwise direction) is low enough to be negligible and a bulk normal velocity exists based on the assumption that the water is impermeable to air [28]:

$$\mathbf{u} \cdot \mathbf{n}_{ws} = -\frac{D}{1 - Y_{ws}} \frac{\partial Y}{\partial n}\Big|_{ws} \tag{14}$$

where $\mathbf{n}_{ws}$ is the water surface's normal vector [m].
Furthermore, Blázquez et al. [10] use a slip boundary condition following the assumption that the concentration boundary layer is thinner than the dynamic boundary layer since the turbulent Schmidt number of the air is lower than unity. Finally, the water vapor flux at the surface can be fixed based on correlations as proposed by Ciuman and Lipska [7], which is not of interest here since the goal is to predict it.
Several authors have measured the friction velocity of the air over a water surface in a wind tunnel [11–14], agreeing on the following empiric correlations:

$$\begin{cases} u_* = 0.05\, U_\infty & \text{if} \quad U_\infty < U_L = 3 \text{ m.s}^{-1} \\ u_* = 0.02\, U_\infty^{\frac{3}{2}} & \text{else} \end{cases} \tag{15}$$

where u_* is the friction velocity and U_L is the air velocity limit above which a distilled water surface transitions from flat to wavy. This criterion may change with the water composition [12]. However, in the case of drying water spans, the wind velocity is often lower than unity, which is far from this threshold.
The friction velocity is defined as follows [29]:

$$u_* = \sqrt{\frac{\tau_s}{\rho}} \tag{16}$$

where τ_s is the shear stress of the fluid over a surface S [Pa]:

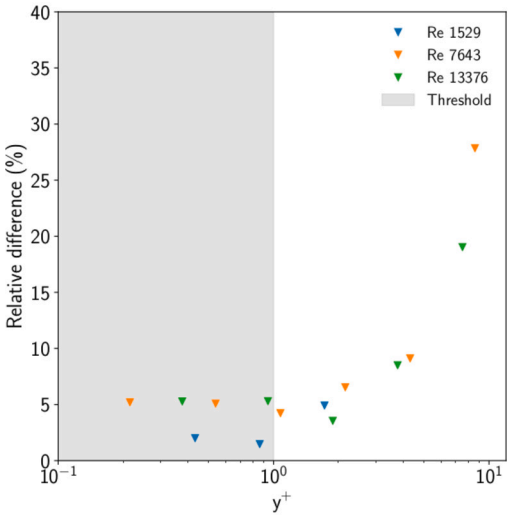

Fig. 3. Relative difference as a function of mesh's y^+, conducted on the Blázquez et al. [30] setup. The blue triangles represent the relative error with $Re_h = 1529$ and $Ri_C = 2.39$, the orange ones with $Re_h = 7643$ and $Ri_C = 0.15$ and the green ones with $Re_h = 13376$ and $Ri_C = 0.06$. The grey zone is the respected criterion for the upcoming simulations. (For interpretation of the colors in the figure(s), the reader is referred to the web version of this article.)

$$\tau_s = \mu \frac{\partial u_t}{\partial n}\Big|_S \tag{17}$$

with μ the laminar dynamic viscosity of the mixture [Pa.s] and $\frac{\partial u_t}{\partial n}|_s$ the surface tangential velocity normal gradient [s^{-1}].
From Equations (16)-(17), one can see the link between u_* and the surface tangential velocity u_t. Thus, the velocity boundary condition proposed in this work is the following:

- The normal velocity is the same as the one used by Raimundo et al. [9] (Equation (14)),
- The tangential velocity (along the streamwise direction) is computed from the friction velocity of the wind over the surface of a water span using Equations (15)-(17).

The slip boundary condition proposed by Blázquez et al. [10] is easier to implement, however it is sensitive to the convection regime [30], hence this boundary condition has been developed.

2.4. Numerical methods

Simulations are carried out using OpenFOAM, a massively parallel open-source CFD software having a large user base [31]. As in Limane et al. [8], the developed solver is a modified version of an existing solver, used for heat transfer in flows using the Boussinesq approximation. The water vapor transport (Equation (7)) and its effect on the density have been added to this solver, while boundary conditions have been developed to compute the interface velocity boundary condition and the turbulent mass transfer wall function.
The developed solver uses the SIMPLE algorithm to solve the flow under steady conditions. Second-order spatial and temporal schemes have been used. Convergence is deemed to be reached when the sum of the residuals for each equation drops below 10^{-5} for each equation. A transient variant has also been developed, based on a PIMPLE algorithm, and is employed to address flow dynamics in unsteady scenarios, particularly in cases involving the formation of unstable convective plumes near the air-water interface.

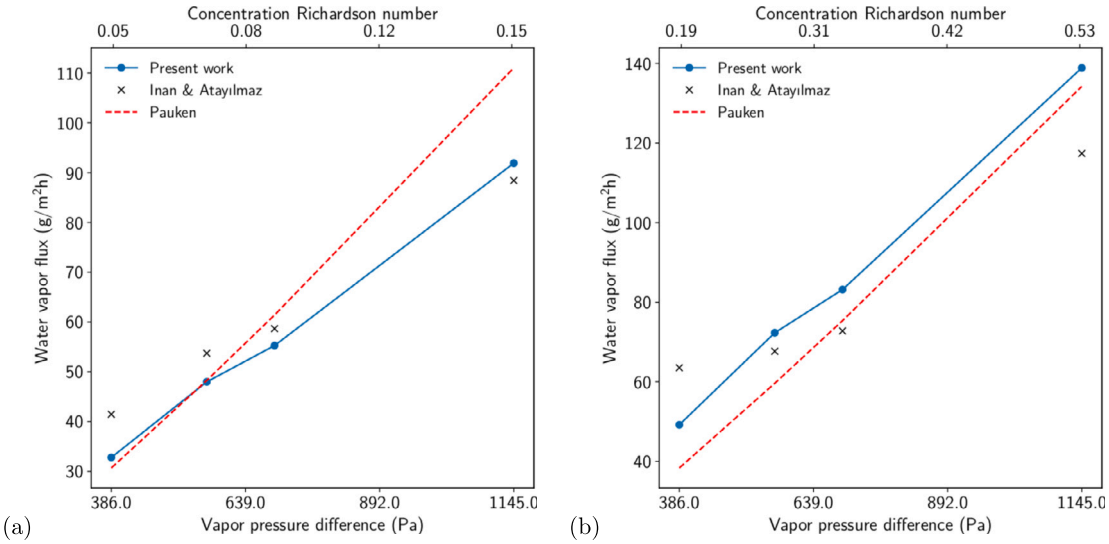

Fig. 4. Comparisons of experimental and numerical water vapor fluxes in the Inan and Atayılmaz [18] configuration, for different flow conditions: (a) Re = 5096 and (b) Re = 9682. The crosses represent the experimental points from Inan and Atayılmaz [18], the red dashed line is the water vapor flux obtained from Pauken's correlation [16] and the blue points are those obtained numerically with the boundary condition proposed in this work.

3. Results and discussion

3.1. Mesh convergence

A mesh refinement investigation is realized to make sure that the results are not sensitive to the grid resolution. Three Reynolds numbers have been considered in the setup studied by Blázquez et al. [30]: $Re_h = 1529$, $Re_h = 7643$ and $Re_h = 13376$, and a concentration Richardson number of $Ri_C = 2.39$, $Ri_C = 0.15$ and $Ri_C = 0.06$ respectively to make sure the flow conditions would not influence the criterion.
As shown in Fig. 3, the relative difference is nearly insensitive to the mesh's resolution when the y^+ criterion is below 1. Hence, the simulations will be carried out on meshes that respect this criterion, agreeing well with the common recommendations when using the SST turbulence model.

3.2. Two dimensional setups

3.2.1. Inan and Atayılmaz setup

The first simulated setup is the one from Inan and Atayılmaz [18]. In this setup, the concentration Richardson number Ri_C ranges from 0.05 to 0.53 under two wind velocities corresponding to $Re_h = 5096$ and $Re_h = 9682$. The comparison between the measured evaporation rates and the simulated ones is shown in Fig. 4, where Pauken's correlation has been added as it is the one with the best agreement to experimental results. Since the measurement uncertainty given by the author is less than 1%, no error bars are shown in the figure. The simulated points are, overall, closer to the measured points than the correlation. The relative difference $D_{r,i}$ between a simulated data set and the corresponding experimental flux in the configuration i is evaluated as:

$$D_{r,i} = \left| \frac{J_{\text{exp},i} - J_{\text{num},i}}{J_{\text{exp},i}} \right| \tag{18}$$

In addition, for a series of N configurations, we evaluate the mean relative difference $D_{r,m}$ as:

$$D_{r,m} = \frac{1}{N} \sum_{i=1}^{N} D_{r,i} \tag{19}$$

In this first 2D series of flow configuration, $D_{r,i}$ varies between 3.93% and 22.6%, with a $D_{r,m}$ of 12.92%.

3.2.2. Blàzquez et al. setup ($0.026 < Ri_C < 3.12$)

The second simulated setup is the one from Blázquez et al. [30]. Additional experimental data are available in Gallero et al. [32], and are discussed in section 3.2.3. Here, Ri_C ranges from 0.0259 to 3.12 and Re_h from 1529 to 10510. The comparison between the set of experimental data, which has a measurement uncertainty of 7%, and the simulations is shown in Fig. 5. The simulation points obtained by the authors, using a slip boundary condition for the near water surface velocity, are also provided. They obtain a maximum relative difference of 44.27% and their mean relative difference is 18.97%. For this initial set of data points utilizing the proposed boundary condition, the values for the relative difference $D_{r,i}$ are within the range of 0.41% to 57.52% and $D_{r,m} = 10.64\%$. Two points from Fig. 5b, at $Ri_C = 0.1579$ and $Ri_C = 0.234$, are clearly deviant from the neighbor points. Removing these two points brings the maximum relative difference from 57.52% to 26% and lowers the mean relative difference $D_{r,m}$ to 8.87%. Anyhow, the boundary condition used in the present paper shows a lower average relative difference than the simple slip condition used in Blázquez et al. [30].

3.2.3. Blàzquez et al. setup ($0.013 < Ri_C < 0.063$)

The second batch of data, obtained from the same setup as in section 3.2.2, is provided in Gallero et al. [32] and Blázquez et al. [22], with Re_h ranging from 13376 to 19490 and Ri_C from 0.013 to 0.063. The objective of these two studies was to enhance the model introduced by Blázquez et al. [10], with a specific emphasis on the forced convection regime, where the slip boundary condition exhibits the poorest performance.
In Gallero et al. [32], the authors use empirical shear stress at the air-water interface fitted from the experimental data, achieving an average relative difference smaller than 5% for the forced convection regime. In Blázquez et al. [22], the slip boundary condition is still used and the turbulent Schmidt number has been changed to better fit the experimental values, achieving an average relative difference of about 7% for the forced convection regime. Although both of these models were initially developed using data from the forced convection regime, they have also been extended to cover other convection regimes. Subsequently, they have been compared to existing data to validate their applicability across a broader range of conditions. Gallero et al. [32] observe a worse behavior in the mixed convection regime than with the slip boundary condition and Blázquez et al. [22] show a high disper-

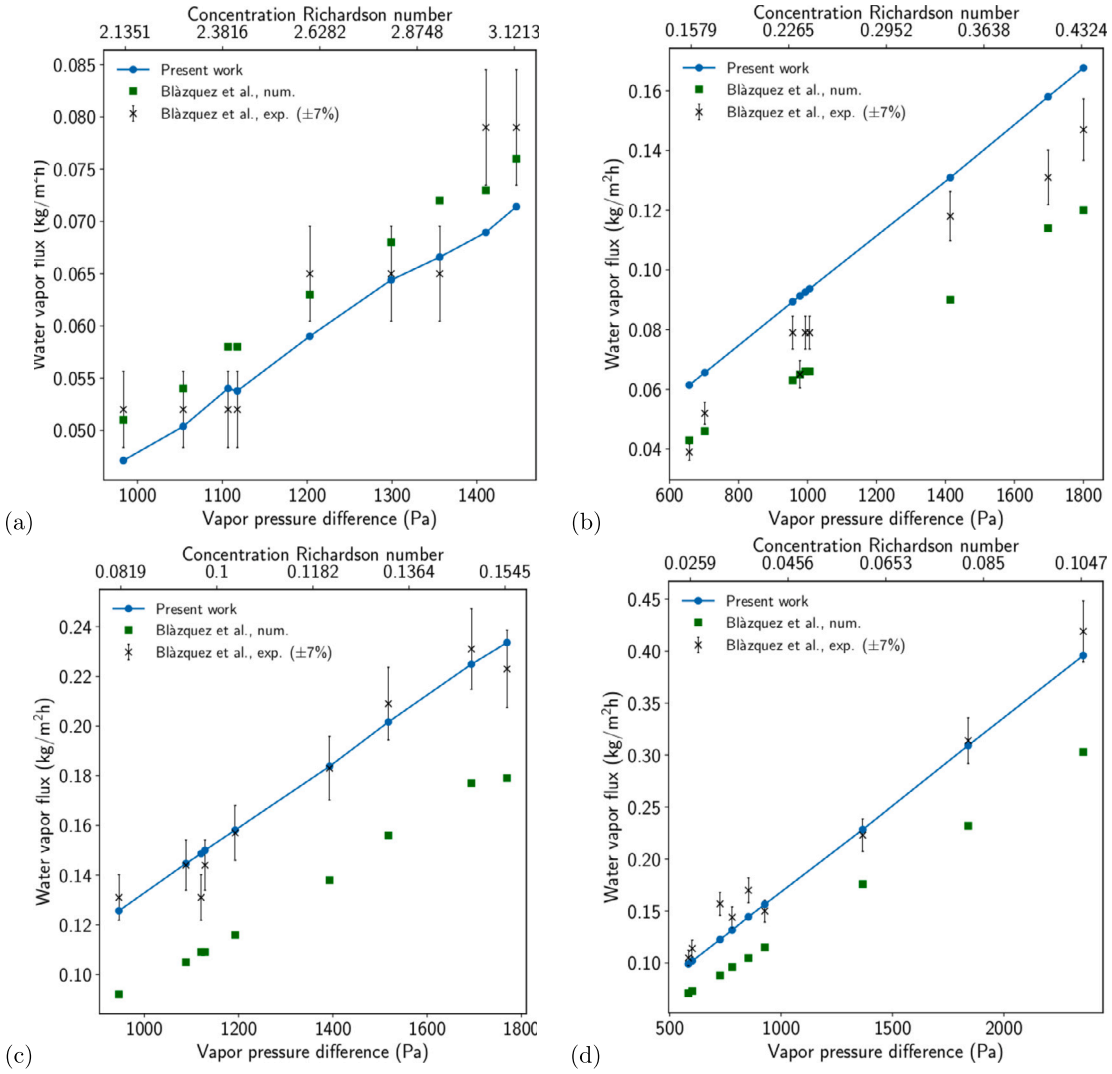

Fig. 5. Comparisons of experimental and numerical water vapor fluxes in the Blàzquez et al. 2D configuration, for different flow conditions: (a) $Re_h = 1529$, (b) $Re_h = 4586$, (c) $Re_h = 7643$ and (d) $Re = 10510$. The crosses represent the experimental points and are associated with a measurement error evaluated in Blázquez et al. [30], the green square points are those obtained numerically by Blázquez et al. [30] with a slip boundary condition, and the blue points are those obtained numerically with the boundary condition proposed in this work.

sion in the mixed convection regime, with a median relative difference of about 19% when $0.1 < Ri_C < 1$.

This additional set is presented in Fig. 6, having a measurement uncertainty of 4% [32], and it is compared to the numerical computation with the model proposed in this paper. Gallero et al. [32] and Blázquez et al. [22] use the same experimental setup with the same inlet velocities, showing similarity between their measurements except at the highest Re_h, as illustrated in Fig. 6c. As the water vapor flux is not expected to deviate between two neighbor points, the relative difference $D_{r,i}$ has been computed based on Gallero et al. [32] experimental data. Then, $D_{r,i}$ falls within the range of 5.28% to 14.65%, with $D_{r,m} = 10.84\%$, which is worse than the two previously mentioned models. While these results are less favorable compared to the two previously mentioned models, they are still considered satisfactory. Notably, this model was not solely designed for predicting evaporation in the forced convection regime, which underscores its versatility.

3.3. Three dimensional setup

The unique 3D simulated configuration is the one from Raimundo et al. [9]. This setup is also the only one that has a higher water temperature than the air, which means that the temperature gradient will also contribute to the water evaporation flux.

In this last setup, Ri_C is between 0.03 and 4.79, Ri_T is between 0.05 and 11.85 and Re_h is between 2548 and 17834. As done for the previous configurations, Fig. 7 shows the comparison between the measured data and the simulated one. No error bars are shown in the figures since the measurement uncertainty is low ($\pm 4 \times 10^{-3}$ g.s^{-1}.m^2). Unlike the previous setups, here the vapor pressure difference is controlled by the water temperature. From Fig. 8, we can notice that increasing the water temperature increases the vapor pressure difference and thus the water vapor flux. Two sets of parameters satisfy $Ri_T > 10$, which is the limit above which the natural convection is completely driving the evaporation process [16]. Under this regime, unstable plumes are noticed in the simulation, preventing its convergence in steady simulations. On the Fig. 7, the grey points are the ones where the unsteady condition is met, and they have been excluded from the computation of the relative differences. Then, for this set of data, $0.3\% < D_{r,i} < 29\%$ and $D_{r,m} = 12.3\%$, which is close to the results obtained in the two-dimensional simulations. From their numerical model, Raimundo et al. [9] have obtained a maximum relative difference of 31.6%, a minimum of 0.3%, and an average of 7.6%. Their model seems to be performing better on aver-

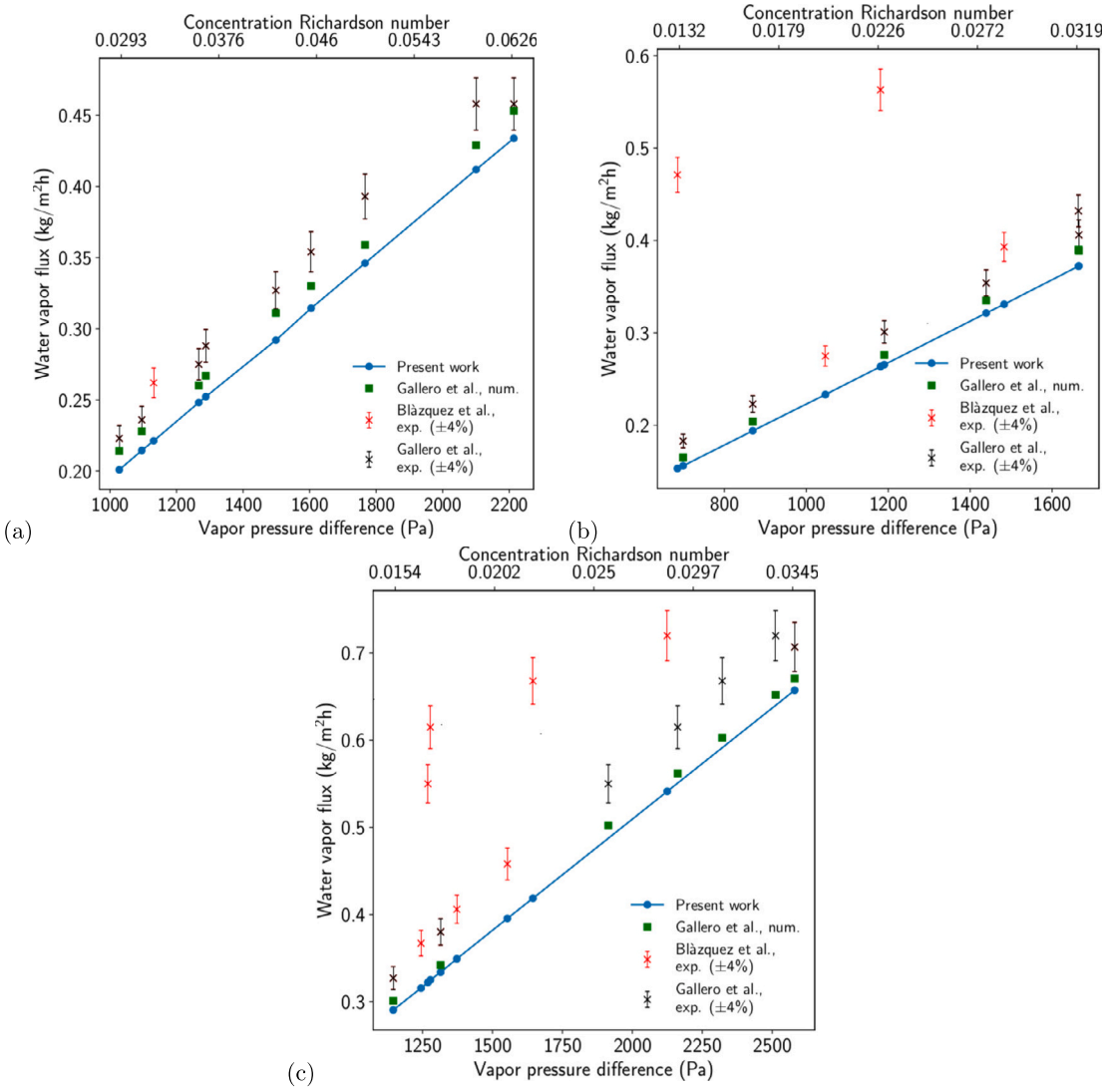

Fig. 6. Comparisons of experimental and numerical water vapor fluxes in the Blàzquez et al. 2D configuration, for different flow conditions: (a) $Re_h = 13376$, (b) $Re_h = 16242$ and (c) $Re_h = 19490$. The black crosses represent experimental points and are associated with a measurement error evaluated in Gallero et al. [32], the red crosses are experimental points from Blázquez et al. [22], the green square points are those obtained numerically by Gallero et al. [32] and the blue points are those obtained numerically with the boundary condition proposed in this work.

age, however, the turbulent Schmidt number was calibrated to better suit their experimental data. Fig. 8 is a visualization of the evolution of the magnitude of the velocity when increasing the water temperature, which highlights the deviation of the velocity streamlines because of the buoyancy to the point where the flow is completely dominated by the latter (Fig. 8c).

3.3.1. On the symmetry boundary condition

As done in Raimundo et al. [9], only half of the wind tunnel is simulated by assuming that both halves of the wind tunnel (along the stream-wise direction) behaved the same, which needs to be checked. Fig. 9 shows the difference between the temperature and water vapor concentration fields close to the water pan when simulating the whole setup (Fig. 9a) and when assuming the symmetry (Fig. 9b). While there are noticeable differences in the flow structures, these disparities have a minimal impact on the water evaporation rate. The relative difference is less than 0.5% when comparing the flux calculated from the entire setup to that calculated from only half of it using symmetry. Additionally, it's important to highlight that the full setup simulation still exhibits symmetry along the same axis as the case where only half of the setup is simulated. This is why the water vapor flux was still computed in the latter scenario.

The pool width not being the same as the wind tunnel's, concentration (and temperature) tubes are observed on the edges of the water span, highlighting the necessity of a three dimensional simulation.

3.3.2. On the natural convection regime

As previously discussed, two experimental points are in the natural convection regime. As expected, it is not possible to compute a steady numerical solution. To evaluate the water vapor flux, it is necessary to simulate the transient flow, at a significantly higher computational cost than the steady simulation, and the flux must be averaged over an appropriate time window. The boundary condition proposed in this work intrinsically assumes that the mixture velocity close to the water surface depends on the inlet air velocity. However, when transitioning to natural convection, this assumption may warrant further consideration, primarily due to the magnitude of the velocity of the rising plumes, as shown in Fig. 8c. Fig. 10 compares the instantaneous flux obtained with the present boundary condition (blue line) and the one obtained by considering a null tangential velocity (orange line). As suggested, removing the near-water velocity dependency on the inlet velocity (in the natural convection regime) brings the mean numerical flux much closer to the

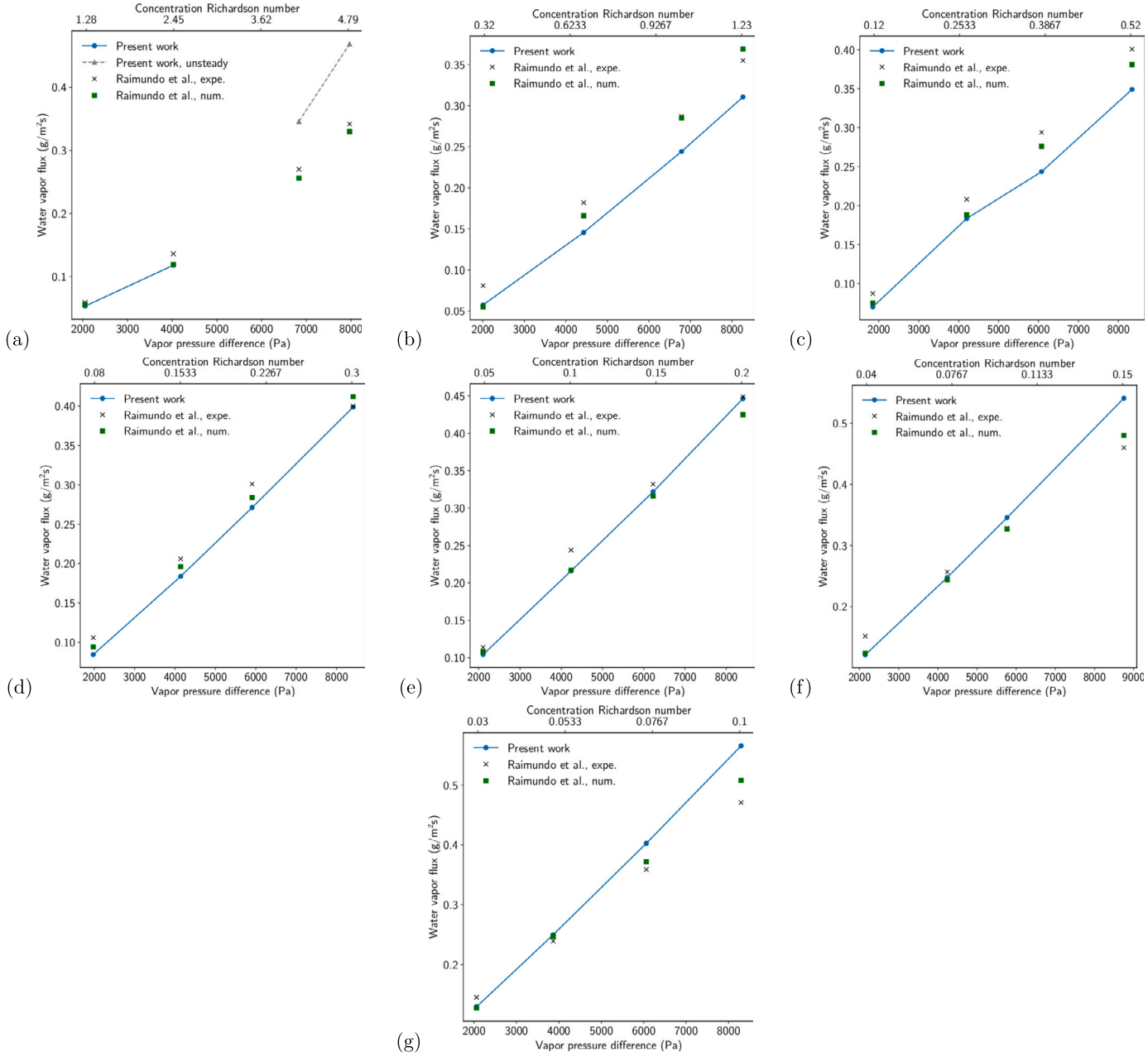

Fig. 7. Comparisons of experimental and numerical water vapor fluxes in the Raimundo et al. 3D configuration, for different flow conditions: (a) $Re_h = 2548$, (b) $Re_h = 5096$, (c) $Re_h = 7643$, (d) $Re_h = 10191$, (e) $Re_h = 12739$, (f) $Re_h = 15287$ and (g) $Re_=17834$. The crosses represent the experimental points, the green square points are those obtained numerically by Raimundo et al. [9] with a fixed normal velocity boundary condition, the grey points are those obtained numerically with the boundary condition proposed in this work under unsteady conditions and the blue points are the ones obtained under steady conditions.

measured flux (black solid line against the grey one). Moreover, periods are observed on the orange flux, underlining the predominant effect of the release of the thermal-concentration plumes on the flow.

3.4. Summary

The relative differences previously computed are summed up in Fig. 11, where 2D and 3D results have been separated. The 2D overall mean relative difference is 11.21% and the one for the 3D case is 12.3% (without considering unsteady simulations). A wide range of Richardson numbers (*i.e.* a wide range of temperature, relative humidity and wind velocity) is considered in these simulations, mainly in the forced and mixed regimes.

The results seem insensitive to the mixed and forced convection regimes, unlike the model developed by Blázquez et al. [10] or the empirical correlations proposed in the literature. However, the model seems sensitive to the transition between the mixed and natural convection regime as illustrated in subsection 3.3.2, needing further assessment.

4. Conclusion

A new near-water air velocity boundary condition for the prediction of the water evaporation rate from a water tank has been developed. This boundary condition uses the empirical friction velocity at the air-water interface to estimate the velocity gradient in the streamwise direction, and the velocity in the normal direction of the water surface is based on the low diffusivity of the air in liquid water. Numerical water vapor flux predictions from several experimental setups were compared with the experimental references. Over the mixed and

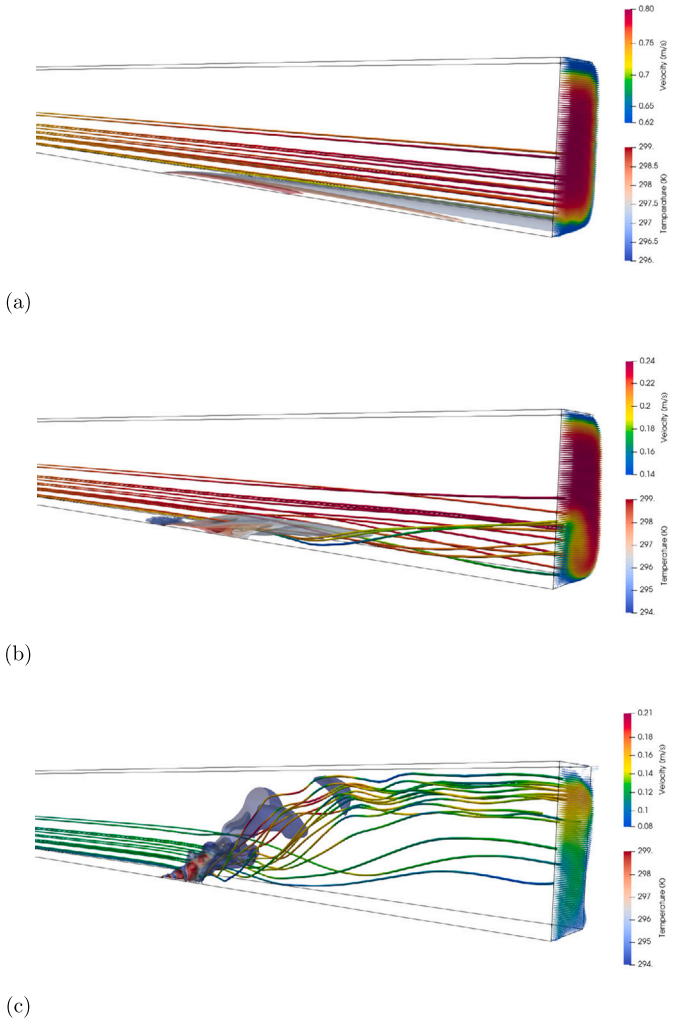

Fig. 8. Temperature and velocity (magnitude) fields, in the 3D configuration of Raimundo et al. [9], side view where (a) $Ri_T = 0.22$, (b) $Ri_T = 2.88$ and (c) $Ri_T = 11.85$. Convergence is reached in (a) and (b), but the case is unsteady in (c).

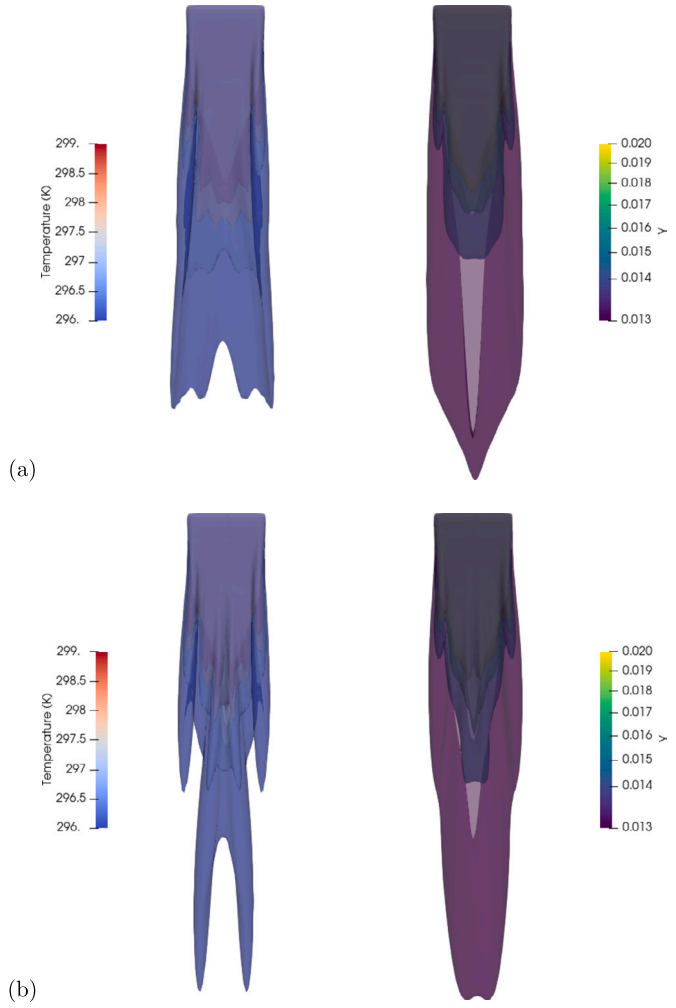

Fig. 9. Temperature and concentration fields, in the 3D configuration of Raimundo et al. [9], top view close to the water pan with $Re_h = 5096$ and $Ri_C = 1.23$, (a) full geometry and (b) half of geometry with symmetry boundary condition (symmetrized field for representation).

forced convection regimes, a mean relative difference close to 12% between experimental and simulated data has been evaluated for both 2D and 3D simulations.

The natural convection regime was only observed in the 3D case due to differences in temperature between the inlet air and the water surface. Temperature drives both thermal and concentration buoyancy, with higher water surface temperatures leading to higher maximum water vapor mass fractions. The density variations induced by the temperature difference are greater than the ones caused by the water vapor concentration difference.

Once reaching this regime, the flow becomes unsteady because of the unstable plumes. In the current study, the limited amount of data available hinders the formation of a robust conclusion regarding the prediction of water vapor flux within the natural convection regime. However, by assuming that the convection plumes are driving the flow under this regime, the friction velocity at the water surface is no longer a function of the mean inlet velocity. This assumption shows good preliminary results.

CRediT authorship contribution statement

Quentin Royer: Conceptualization, Methodology, Software, Validation, Writing – original draft, Writing – review & editing. **Romain Guibert:** Supervision, Writing – original draft, Writing – review & editing. **Pierre Horgue:** Supervision, Writing – original draft, Writing – review & editing. **Adam Swadling:** Supervision. **Gérald Debenest:** Supervision, Writing – original draft, Writing – review & editing.

Declaration of competing interest

The authors declare the following financial interests/personal relationships which may be considered as potential competing interests: Quentin Royer reports financial support was provided by the National Association of Research and Technology (ANRT). If there are other authors, they declare that they have no known competing financial interests or personal relationships that could have appeared to influence the work reported in this paper.

Data availability

Data will be made available on request.

Acknowledgements

This study was carried out as part of a PhD work funded by Safetykleen and the National Association of Research and Technology (ANRT) under the Cifre contract n°2023/0076. It was granted access to the HPC resources of CALMIP supercomputing center under the allocation p21016.

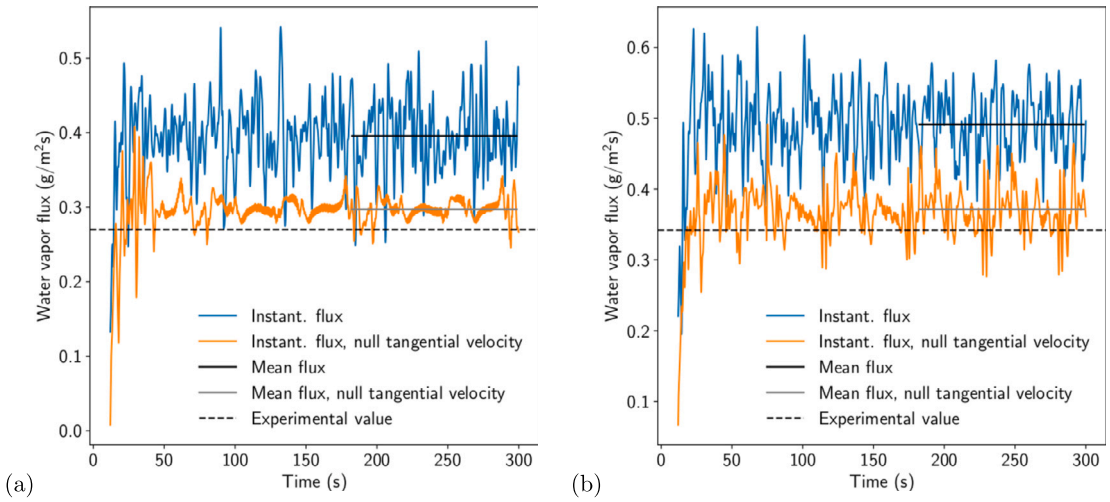

Fig. 10. Instantaneous visualization of the water vapor flux in the 3D configuration of Raimundo et al. [9], (a) $Re_h = 2548$, $Ri_T = 10.34$ and (b) $Re_h = 2548$, $Ri_T = 11.85$. The blue line is the instantaneous water vapor flux with the boundary proposed in this work, the orange line is the water vapor flux where the streamwise velocity is killed, the black line is the average water vapor flux numerically measured on the blue line, the grey line is the average water vapor flux numerically measured on the orange line and the dark dashed line is the measured water vapor flux.

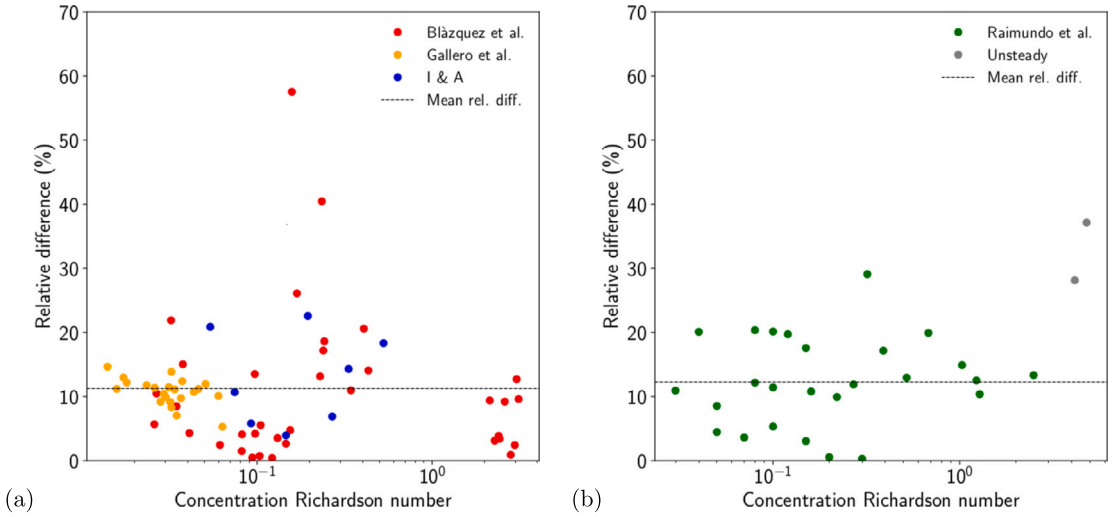

Fig. 11. Relative difference between experimental and simulated data as a function of the concentration Richardson number, (a) 2D cases and (b) 3D case. Red, green, orange and blue dots are the relative difference under steady conditions, grey dots are the relative difference under unsteady conditions and the dotted line is the mean relative difference.

References

[1] P. Sun, J.Y. Wu, R.Z. Wang, Y.X. Xu, Analysis of indoor environmental conditions and heat pump energy supply systems in indoor swimming pools, Energy Build. 43 (5) (2011) 1071–1080, https://doi.org/10.1016/j.enbuild.2010.08.004.

[2] D. Kong, H. Liu, Y. Wu, B. Li, S. Wei, M. Yuan, Effects of indoor humidity on building occupants' thermal comfort and evidence in terms of climate adaptation, Build. Environ. 155 (2019) 298–307, https://doi.org/10.1016/j.buildenv.2019.02.039.

[3] P.S. Chauhan, A. Kumar, B. Gupta, A review on thermal models for greenhouse dryers, Renew. Sustain. Energy Rev. 75 (2017) 548–558, https://doi.org/10.1016/j.rser.2016.11.023.

[4] F.P. Incropera, D.P. DeWitt, T.L. Bergman, A.S. Lavine, Fundamentals of Heat and Mass Transfer, Wiley, 2007.

[5] J. Dalton, Experimental essays on the constitution of mixed gases, on the force of steam or vapour from water and other liquids in different temperatures, both in a Torricellian vacuum and in air, on evaporation, and on the expansion of gases, in: Memoirs of the Literary and Philosophical Society of Manchester, 1802.

[6] S. Aldarabseh, Evaporation Rate from Free Water Surface, Dissertations, 2020.

[7] P. Ciuman, B. Lipska, Experimental validation of the numerical model of air, heat and moisture flow in an indoor swimming pool, Build. Environ. 145 (2018) 1–13, https://doi.org/10.1016/j.buildenv.2018.09.009.

[8] A. Limane, H. Fellouah, N. Galanis, Simulation of airflow with heat and mass transfer in an indoor swimming pool by OpenFOAM, Int. J. Heat Mass Transf. 109 (2017) 862–878, https://doi.org/10.1016/j.ijheatmasstransfer.2017.02.030.

[9] A.M. Raimundo, A.R. Gaspar, A.V.M. Oliveira, D.A. Quintela, Wind tunnel measurements and numerical simulations of water evaporation in forced convection airflow, Int. J. Therm. Sci. 86 (2014) 28–40, https://doi.org/10.1016/j.ijthermalsci.2014.06.026.

[10] J.L.F. Blázquez, I.R. Maestre, F.J.G. Gallero, P.Á. Gómez, A new practical CFD-based methodology to calculate the evaporation rate in indoor swimming pools, Energy Build. 149 (2017) 133–141, https://doi.org/10.1016/j.enbuild.2017.05.023.

[11] R.G. Vines, Wind stress on a water surface: measurements at low wind speeds with the aid of surface films, Q. J. R. Meteorol. Soc. 85 (364) (1959) 159–162, https://doi.org/10.1002/qj.49708536409.

[12] J.C. Gottifredi, G.J. Jameson, The growth of short waves on liquid surfaces under the action of a wind, Proc. R. Soc. Lond. Ser. A, Math. Phys. Sci. 319 (1538) (1970) 373–397.

[13] W.J. Plant, J.W. Wright, Growth and equilibrium of short gravity waves in a wind-wave tank, J. Fluid Mech. 82 (4) (1977) 767–793, https://doi.org/10.1017/S0022112077000974.

[14] S. Komori, R. Nagaosa, Y. Murakami, Turbulence structure and mass transfer across a sheared air–water interface in wind-driven turbulence, J. Fluid Mech. 249 (1993) 161–183, https://doi.org/10.1017/S0022112093001120.

[15] K. Takeishi, G. Kawahara, H. Wakabayashi, M. Uhlmann, A. Pinelli, Localized turbulence structures in transitional rectangular-duct flow, J. Fluid Mech. 782 (2015) 368–379, https://doi.org/10.1017/jfm.2015.546.
[16] M.T. Pauken, An experimental investigation of combined turbulent free and forced evaporation, Exp. Therm. Fluid Sci. 18 (4) (1998) 334–340, https://doi.org/10.1016/S0894-1777(98)10038-9.
[17] A. Jodat, M. Moghiman, M. Anbarsooz, Experimental comparison of the ability of Dalton based and similarity theory correlations to predict water evaporation rate in different convection regimes, Heat Mass Transf. 48 (8) (2012) 1397–1406, https://doi.org/10.1007/s00231-012-0984-z.
[18] M. Inan, Ş Atayılmaz, Experimental investigation of evaporation from a horizontal free water surface, SIGMA (2017).
[19] J. Boussinesq, Théorie analytique de la chaleur mise en harmonie avec la thermodynamique et avec la théorie mécanique de la lumière, Tome 2, Gauthier-Villars, 1901.
[20] J.H. Lienhard, A Heat Transfer Textbook, Dover Publications, Mineola, N.Y, 2011.
[21] F.R. Menter, Two-equation eddy-viscosity turbulence models for engineering applications, AIAA J. 32 (8) (1994) 1598–1605, https://doi.org/10.2514/3.12149.
[22] J.L.F. Blázquez, I.R. Maestre, F.J.G. Gallero, L. Pérez-Lombard, M. Bottarelli, Experimental adjustment of the turbulent Schmidt number to model the evaporation rate of swimming pools in CFD programmes, Case Stud. Therm. Eng. 41 (2023) 102665, https://doi.org/10.1016/j.csite.2022.102665.
[23] Y. Tominaga, T. Stathopoulos, Turbulent Schmidt numbers for CFD analysis with various types of flowfield, Atmos. Environ. 41 (37) (2007) 8091–8099, https://doi.org/10.1016/j.atmosenv.2007.06.054.
[24] C.C. Chieng, B.E. Launder, On the calculation of turbulent heat transport downstream from an abrupt pipe expansion, Numer. Heat Transf. (2007), https://doi.org/10.1080/01495728008961754.
[25] C.L.V. Jayatilleke, The influence of Prandtl number and surface roughness on the resistance of the laminar sub-layer to momentum and heat transfer, Ph.D., University of London, 1966.
[26] M. Knudsen, The Kinetic Theory of Gases: Some Modern Aspects, Methuen, 1946.
[27] A.L. Buck, New equations for computing vapor pressure and enhancement factor, J. Appl. Meteorol. Climatol. 20 (12) (1981) 1527–1532, https://doi.org/10.1175/1520-0450(1981)020<1527:NEFCVP>2.0.CO;2.
[28] L.C. Burmeister, Convective Heat Transfer, John Wiley & Sons, 1993.
[29] H. Schlichting, K. Gersten, Boundary-Layer Theory, Springer, Berlin, Heidelberg, 2017.
[30] J.L.F. Blázquez, I.R. Maestre, F.J.G. Gallero, P.Á. Gómez, Experimental test for the estimation of the evaporation rate in indoor swimming pools: validation of a new CFD-based simulation methodology, Build. Environ. 138 (2018) 293–299, https://doi.org/10.1016/j.buildenv.2018.05.008.
[31] H.G. Weller, G. Tabor, H. Jasak, C. Fureby, A tensorial approach to computational continuum mechanics using object-oriented techniques, Comput. Phys. 12 (6) (1998) 620–631, https://doi.org/10.1063/1.168744.
[32] F.J.G. Gallero, I.R. Maestre, J.L.F. Blázquez, J.D.M. Baladés, Enhanced CFD-based approach to calculate the evaporation rate in swimming pools, Sci. Technol. Built Environ. 27 (4) (2021) 524–532, https://doi.org/10.1080/23744731.2020.1868219.